



Asymmetric embedded benzene ring enhances charge transfer of carbon nitride for photocatalytic hydrogen generation



Guangri Jia^a, Ying Wang^a, Xiaoqiang Cui^{a,*}, Zhenxing Yang^b, Lulu Liu^a, Haiyan Zhang^a, Qiong Wu^a, Lirong Zheng^c, Weitao Zheng^{a,*}

^a State Key Laboratory of Automotive Simulation and Control, School of Materials Science and Engineering, Key Laboratory of Automobile Materials of MOE, Jilin University, 2699 Qianjin Street, Changchun 130012, PR China

^b State Key Laboratory of Superhard Materials, College of Physics, Jilin University, 2699 Qianjin Street, Changchun 130012, PR China

^c Institute of High Energy Physics, Beijing Synchrotron Radiation Facility, Chinese Academy of Sciences, Beijing 100190, PR China

ARTICLE INFO

Keywords:

g-C₃N₄
Water splitting
2D material
Hydrogen evolution
Benzene ring

ABSTRACT

Preventing the high carrier recombination rate of graphitized C₃N₄ (GCN) is an urgent problem to be solved for its application as a photocatalyst for hydrogen production. Here, we first rationally embed the benzene ring in GCN to modify the local symmetry without changing its long-order structure. Theoretical calculation predicts that this design can change the electronic structure and promote the effective charge transfer in GCN. The benzene ring embedded GCN is successfully prepared by copolymerization using dicyandiamide and terephthalonitrile as precursors. Photoluminescence (PL) and time-resolved transient PL (TRPL) spectra confirm that the electron transfer efficiency of the benzene ring embed GCN is greatly improved. This nanomaterial displays 10.8 times higher photocatalytic hydrogen production rate than that of pristine GCN with the apparent quantum yield of 11.3% at 400 nm and 9% at 420 nm. This work provides a novel strategy for designing high-efficiency two-dimensional (2D) photocatalytic materials for water splitting.

1. Introduction

Developing cost-effective, environmentally benign, high-efficiency and stable visible light photocatalysts is the key issue for converting abundant solar energy into storable and sustainable chemical fuels [1–3]. Researchers have contributed many efforts on the three aspects of catalysts to improve their performances: 1) the utilization of whole solar energy spectrum [4–6]; 2) the separation efficiency of photo-induced carriers [7–9]; and 3) the interfacial chemical reaction active sites [10–12]. The above functions can be adjusted by changing the material electronic structure of photocatalysts. Among various semiconductor materials, graphite carbon nitride (GCN), as a prototypical two-dimensional (2D) layered conjugated polymer, was widely studied due to its robust stability, suitable bandgap structure, good photo-corrosion resistance, and easy preparation [13–15]. However, the high recombination rate of photoinduced carriers of pristine GCN still hinders the interfacial reaction of photocatalysis [16–18]. And the poor electrical conductivity also greatly restricts the electron transfer for the reaction involving photogenerated carriers [19,20].

To overcome these inherent disadvantages, some strategies have been implemented, including doping, morphological regulation, band

regulation, use of co-catalysts, and heterojunction with other semiconductors [21–24]. Recently, preparation of GCN with symmetrical benzene ring embedding had been developed as a promising way to obtain high-performance visible-light-induced GCN photocatalyst [25–27]. We assumed that using benzene ring to partly replace the heptazine structure of GCN will destroy the local symmetry of GCN and result in the electronic structure variation from the pristine GCN [28]. This localized asymmetry of the structure leads to the formation of separate positive and negative charge centers, forming a localized internal field that facilitates the photogenerated carriers separation [7].

Theoretical calculation shows that the localized symmetry of GCN is broken by partially substituting the heptazine ring with an embedded benzene ring, which changes the electronic structure and then promoted the charge transfer, which is confirmed by experimental results of PL and TRPL. The synthesis of the local asymmetry benzene embedding GCN (A-GCN) was implemented by using dicyandiamide and π -rich terephthalonitrile as the precursor at a high-temperature annealing treatment [13]. The fact of benzene ring embedding is confirmed by XPS, FTIR, and ¹³C-NMR characterization. The results of the UV-vis absorption spectrum, valence band XPS (VB-XPS) and electrochemical Mott-Schottky plots show that the band structure of the

* Corresponding authors.

E-mail addresses: xqcui@jlu.edu.cn (X. Cui), wtzheng@jlu.edu.cn (W. Zheng).

material is changed after the benzene ring was embedded. The resultant nanomaterial shows 10 times higher hydrogen evolution (HER) rate than the pristine GCN with stable and efficient performance for H₂ evolution under visible light irradiation ($\lambda > 420$ nm). Our results show that the insertion of benzene ring produces synergistic optical and electronic effects, changes local charge distribution and electron transfer kinetics, and promote the photocatalytic water splitting to produce hydrogen at a higher rate. This work is of great significance for improving the catalytic properties of two-dimensional photocatalytic materials benefitting from the effective charge transfer by regulating the local electronic structure.

2. Experimental section

2.1. Materials

All the chemicals were analytical grade and used as received without further purification. Dicyandiamide and triethanolamine were purchased from the Sinopharm Chemical Reagent Co., Ltd (China). Terephthalonitrile was obtained from Aladdin Industrial Inc (USA). Distilled water was used throughout the experiments.

2.2. Synthesis of photocatalysts

30 mg of dicyandiamide was mixed with a certain amount of terephthalonitrile by grounding. The mixture was then transferred into a covered crucible and heated at 550 °C for 4 h with an increasing rate of 2 °C min⁻¹. And the obtained sample was cooled to room temperature and ground further. A second annealing process was performed at 500 °C for 2 h with an increasing rate of 2 °C min⁻¹.

2.3. Characterization

The powder X-ray diffraction (XRD) was conducted by on a Bragg-Brentano diffractometer (D8-tools, Germany) equipped with a CuK_α source emitting at 0.15418 nm for the compositions of the samples. Transmission electron microscope (TEM) images of the as-prepared samples were acquired by a JEM-2000EX transmission electron microscope (JEOL Co., Japan) with an acceleration voltage of 200 kV. The morphologies of the samples were obtained using a field emission scanning electron microscopy (FESEM) (Hitachi, SU8010, Japan). X-ray photoelectron spectroscopy (XPS) was measured with an ESCALAB-250 instrument (Thermo Fisher Scientific, USA). Fourier transformed infrared (FT-IR) spectroscopies were recorded by a Nicolet IS 10 FT-IR spectrometer, using the KBr wafer technique. The photoluminescence (PL) and time-resolved transient PL (TRPL) spectra were obtained by using an LS55 spectrometer (PerkinElmer Inc., USA) and an Edinburgh FLS920 spectrophotometer using a 360 nm nanosecond pulse laser as the excitation source, respectively. UV-vis spectra were measured on a UV-vis spectrophotometer (Shimadzu, UV-2550, Japan) equipped with an integrated sphere attachment, and BaSO₄ was used as a reference. The inductively coupled plasma mass spectrometry (ICP-MS) results were conducted using an ELAN 9000/DRC system. N₂ adsorption/desorption isotherm was measured at 77 K by using a Quanta 4200e surface area analyzer. The pore size distribution was derived from the adsorption curve by using the Barrett-Joyner-Halenda (BJH) method. And ¹³C solid-state NMR was measured on a Varian Infinityplus 400 spectrometer operating at a magnetic field strength of 9.4 T. Raman spectra were conducted on a micro-Raman spectrometer (HR Evolution) using a 785 nm laser as excitation source at room temperature.

2.4. Photoelectrochemical measurement

The prepared sample was dissolved in 0.5 vol% Nafion solution-ethanol solution and dispersed uniformly by ultrasound. The obtained suspension was applied evenly on the washed FTO conductive glass by

drop coating. Then, a standard three-electrode (work electrode: the prepared sample, the counter electrode: a Pt foil, and reference electrode: an Ag /AgCl composing of saturated KCl) system with 0.5 M Na₂SO₄ electrolyte was conducted. Electrochemical measurements of the prepared sample were conducted by using CHI650D. Electrochemical impedance spectra (EIS) were measured over a frequency range of 10⁵ ~ 10⁻¹ Hz with 10 mV amplitude under visible-light irradiation ($\lambda > 420$ nm).

2.5. Photocatalytic activity

Photocatalytic hydrogen evolution reactions were recorded by a GC2014C gas chromatography system equipped with a thermal conductivity detector, Ar as a carrier gas, and 5 Å molecular sieve column. 10 mg of photocatalyst powder was dispersed uniformly by ultrasound in 50 mL of an aqueous solution containing 10 vol% triethanolamine (TEOA, a hole capturing agent). 3 wt% Pt was deposited on the photocatalyst surface by using an *in-situ* photo-deposition method using H₂PtCl₆ as the platinum source [6]. The suspension of catalysts was then added to a glass container with a top-irradiated quartz glass lid. A 300 W Xe lamp with an optical filter ($\lambda > 420$ nm) was placed above the container. The measured average incident power of light was about 0.06 W cm⁻². In a typical reaction, the reactor container temperature was controlled at 5 °C using a circulating condensate system. Before visible-light irradiation, the suspension was bubbled for 30 min using high-purity Ar gas to remove the dissolved oxygen completely. And the apparent quantum yield (AQY) was calculated using the following equation [24]:

$$AQY = (N_e \times 2)/N_p \times 100\% = (2 \times n \times h \times c)/(P \times S \times t \times \lambda) \times 100\% \quad (1)$$

where the N_e represents the number of reaction electrons, N_p is the number of incident photons, n is evolved H₂ molecules, h is the Planck constant, c is the speed of light, P is the intensity of light in solution, S is the area of light on the solution, t is photocatalytic reaction time, and λ is incident monochromatic light wavelength.

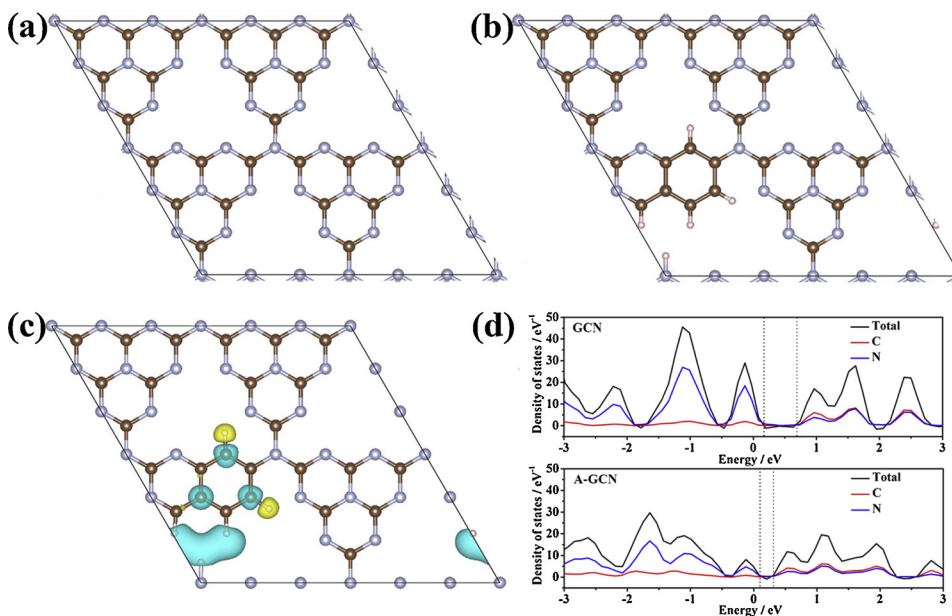
2.6. Theoretical calculations

The calculations were performed by Vienna ab initio Simulation Package (VASP 5.3) with the generalized gradient approximation (GGA) of Perdew-Burke-Ernzerhof (PBE) type exchange-correlation potential. The cut-off energy of the plane wave basis set was set to be the ENMAX value in the pseudo-potential file plus 25%. A Γ -centered $6 \times 6 \times 1$ Monkhorst-Pack grid was used for the self-consistent calculations. To avoid the interlayer interactions, a vacuum spacing in the z-direction was set to be 15 Å.

3. Results and discussion

3.1. Theoretical calculations

The electronic structures of GCN and A-GCN were first investigated by theoretical calculations using VASP. The two-dimensional molecule structures of monolayer GCN and A-GCN are illustrated in Fig. 1a-b. Compared with GCN consisting of heterocyclic rings, a heterocyclic ring is missed in the structural unit, and another heterocyclic ring is replaced by a benzene ring in A-GCN structure. Differential charge density is performed to understand the electron transfer between different atoms directly by subtracting the charge distribution of GCN from that of A-GCN. As shown in Fig. 1c, A-GCN exhibits a significant charge distribution change. The substituted part generates a delocalized charge, and the missing position corresponds to a strong electron loss, which represents a strong positive charge region [25]. Therefore, the benzene ring embedding results in the charge rearrangement and



promotes the charge separation in A-GCN, which is essential to improve the photocatalytic activity [7]. Density of states (DOS) shows that the bandgap of single-layer A-GCN (0.25 eV) is smaller than that of GCN (0.62 eV). Compared with single-layer GCN, the bandgap is decreased after embedding benzene ring. The DOS results of single-layer A-GCN show that N is the dominant valence band, and both N and C are the dominant conduction bands.

3.2. Morphology and structural characterization

A-GCN was synthesized through a thermal polymerization reaction (Scheme S1) [25,29]. The benzene ring embedding amount is changed by adding different amounts of terephthalonitrile. The morphology of A-GCN-*n* (*n* is the grams of terephthalonitrile added) and pristine GCN is characterized by SEM and TEM. The GCN and A-GCN-*n* exhibit two-dimensional sheet-like structure as shown in Figs. 2a–e and S1. The integrity of A-GCN-*n* in-plane is broken due to the influence of the benzene ring. The fact that there are many defective holes in the lamellar layer also proves that external units are embedded. The inset shows the corresponding digital photographs of as-prepared samples. With increasing benzene ring embedding amount, the color of powders changes from light yellow for GCN to dark yellow for A-GCN-1.0. These results indicate that the surface properties of A-GCN-*n* are apparently affected by the embedding amount of benzene ring. XRD in Fig. 2f shows that they are the same structure as GCN ontology, indicating that the main structure is not damaged. The degree of crystallization of the sample is gradually deteriorated with the increase of benzene ring embedding amount, indicating that embedding of benzene ring affects the ordered structure of GCN [30]. High-resolution TEM and selected area electron diffraction also show that the structure of A-GCN is consistent with GCN (Fig. S2). And when *n* is further increased to 2.0, the structure of A-GCN is not retained (Fig. S3). The porous structure and surface area are investigated by nitrogen adsorption-desorption isotherms, which exhibits a type-IV with a hysteresis loop as shown in Fig. 2g [31]. The nitrogen uptake is significantly increased in the high-pressure range with the increase of benzene ring embedding amount, indicating the existence of mesoporous. The Brunauer-Emmett-Teller (BET) surface area of A-GCN-1.0 is approximately $281.7 \text{ m}^2 \text{ g}^{-1}$, which is over five times higher than that of GCN (ca. $51.7 \text{ m}^2 \text{ g}^{-1}$), consistent with the TEM observation (Fig. 2a–e). The pore sizes are mainly distributed around 5.5 nm and 26.5 nm in Fig. 2h, respectively. Such an increased specific surface area of A-GCN-*n* should be beneficial for its

Fig. 1. (a, b) The crystal structure of monolayer GCN and A-GCN, respectively. The blue, black and the red balls in the figure represent the nitrogen, carbon and hydrogen atoms, respectively. (c) Charge density difference of monolayer GCN and A-GCN, blue and yellow represent the charge loss and accumulation, respectively (the isosurface value is set to 0.04 eA^{-3}). (d) The density of states (a, b) of GCN and A-GCN-*n* (the Fermi level is set at zero).

application as photocatalysts, which exposes more active sites to accelerate the occurrence of the surface reaction.

X-ray photoelectron spectroscopy (XPS) is used to characterize the elements oxidation state. The XPS survey of C, N, and O are shown in Fig. S4. The C 1s spectrum exhibit three contributions located at respectively 284.7, 286.1, and 288.3 eV as shown in Fig. 3a–e. The 284.7 eV signal of A-GCN-*n* from the C 1s analysis is ascribed to C=C/C-C groups [32]. With the gradual addition of terephthalonitrile, the proportion of C=C/C-C groups gradually increases, confirming the increase of benzene ring embedding amount. At the same time, as a result of incomplete polymerization, there exists C-NH_x (286.1 eV) on the edges of heptazine units. And N-C = N (288.3 eV) coordination in the framework of A-GCN-*n* further explains the formation of the structure of GCN [33]. The N 1s spectrum can be well fitted to four N species, i.e., the C-N = C (398.8 eV), N-(3C) (399.9 eV), N-H_x (401.3 eV), and π excitation (405.0 eV) of the C=N conjugated structure (Fig. S5) [34]. With the increase of benzene ring amount, the ratio of N-H_x to N gradually decreases (Table S1), which suggests the polymerization of the heptazine unit and terephthalonitrile. The proportion of carbon and nitrogen is correlated with the benzene ring embedding amount from the ICP results (Fig. 3f), which is consistent with the XPS results. The FTIR results in Fig. 3g shows a sharp peak in 813 cm^{-1} , corresponding to the heptazine [35]. The peaks in the range of 1200 – 1700 cm^{-1} belong to the carbon and nitrogen heterocycles. The peaks of 813 cm^{-1} and 1200 – 1700 cm^{-1} gradually become weak with the increase of benzene ring embedding amount due to the partial replacement of heptazine unit by benzene ring. Peaks of C=C (1571 cm^{-1}) and C-C (1435 cm^{-1}) gradually become prominent due to the embedding of the benzene ring [36]. ¹³C solid NMR shows two characteristic peaks of heptazine rings at 157.0 ppm and 165.5 ppm corresponding to C-N₃ and C-N₂(NH_x), respectively. The newly introduced 132.0 ppm is attributed to the aromatic carbon structure in A-GCN-1.0 (Fig. 3h) [29]. The typical vibration of CN heterocycles is also confirmed by the Raman spectrum (Fig. S6). The absence of D band and G band peaks of A-GCN-*n* indicates that there is no carbonization process of the precursor during the preparation of A-GCN-*n*, which once again indicates the integrity and stability of the benzene ring.

3.3. Band structure characterization

The embedding of a benzene ring greatly affects the band structure of A-GCN. We study the effect of different addition amounts of

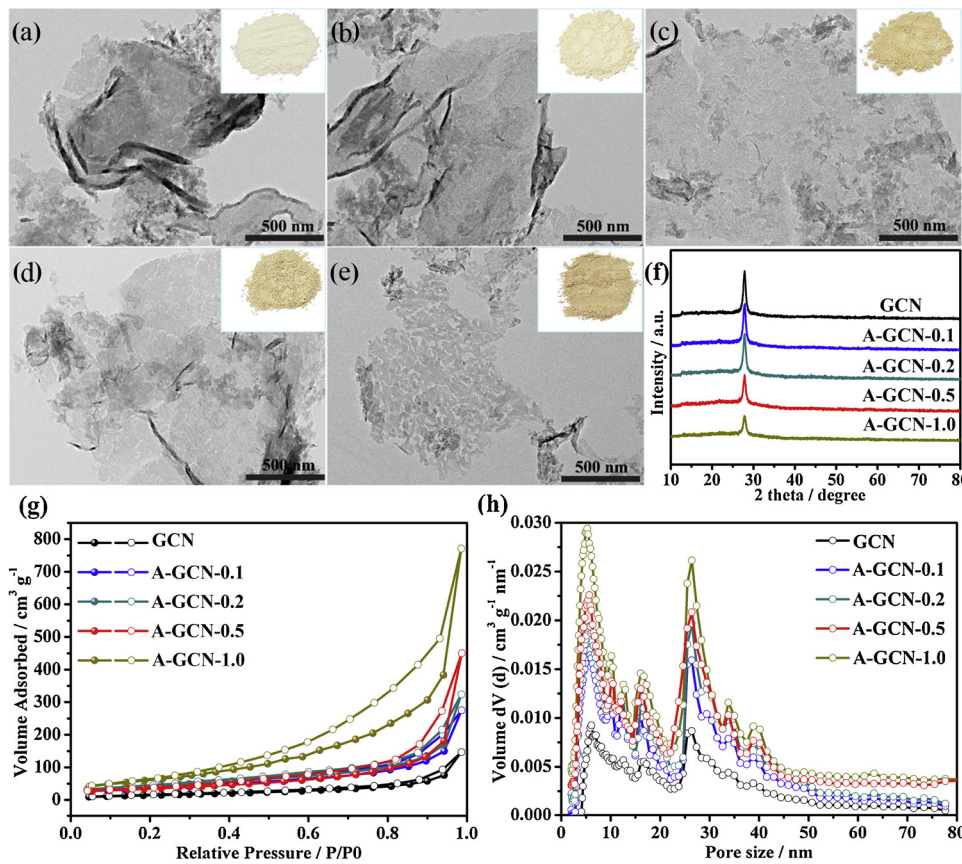


Fig. 2. (a–e) TEM of the GCN, A-GCN-0.1, A-GCN-0.2, A-GCN-0.5, and A-GCN-1.0, and the inset are the corresponding optical picture, (f) the XRD patterns, (g) N_2 -sorption isotherms collected at 77 K, and (h) pore size distribution for the samples. The pore size distribution is determined from the desorption branch of the isotherm.

terephthalonitrile precursors on the bandgap by UV-vis spectra in Fig. 4a. The adsorption shifts from 425 nm to 450 nm, suggesting that the bandgap decreases with the increasing terephthalonitrile [22]. The absorption band tail also increases in the visible region due to the $n-\pi^*$ electron transition [37]. The optical bandgaps of the A-GCN-*n* are

calculated from the Tauc plots [17] (Fig. S7) and summarized in Table S2. The existence of such an absorption peak at about 500 nm is mainly due to the incomplete polymerization during the thermal polymerization process. And the bandgap of theoretical calculation of single-layer GCN is lower than the experimental value, which is due to the

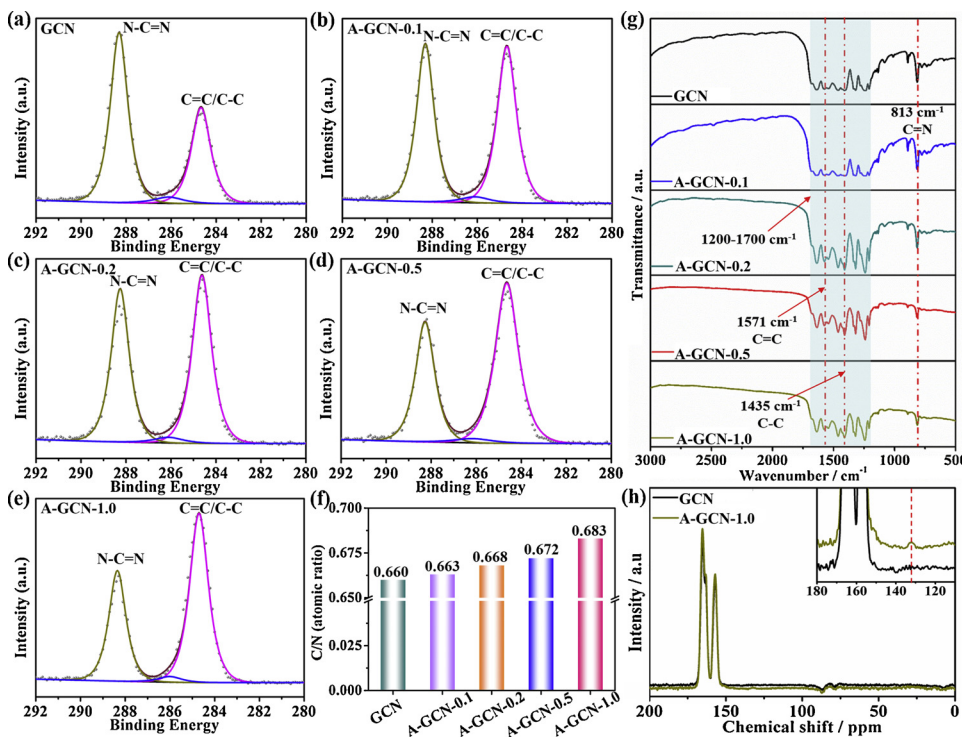


Fig. 3. (a–e) The C 1s XPS spectra, (f) the ratio of carbon to nitrogen from inductively coupled plasma mass spectrometry (ICP-MS), (g) FT-IR spectra of the series of GCN, A-GCN-0.1, A-GCN-0.2, A-GCN-0.5, and A-GCN-1.0, and (h) ^{13}C solid-state NMR spectra of GCN and A-GCN-1.0; inset shows an enlargement around 110–180 ppm in GCN and A-GCN-1.0 spectrum.

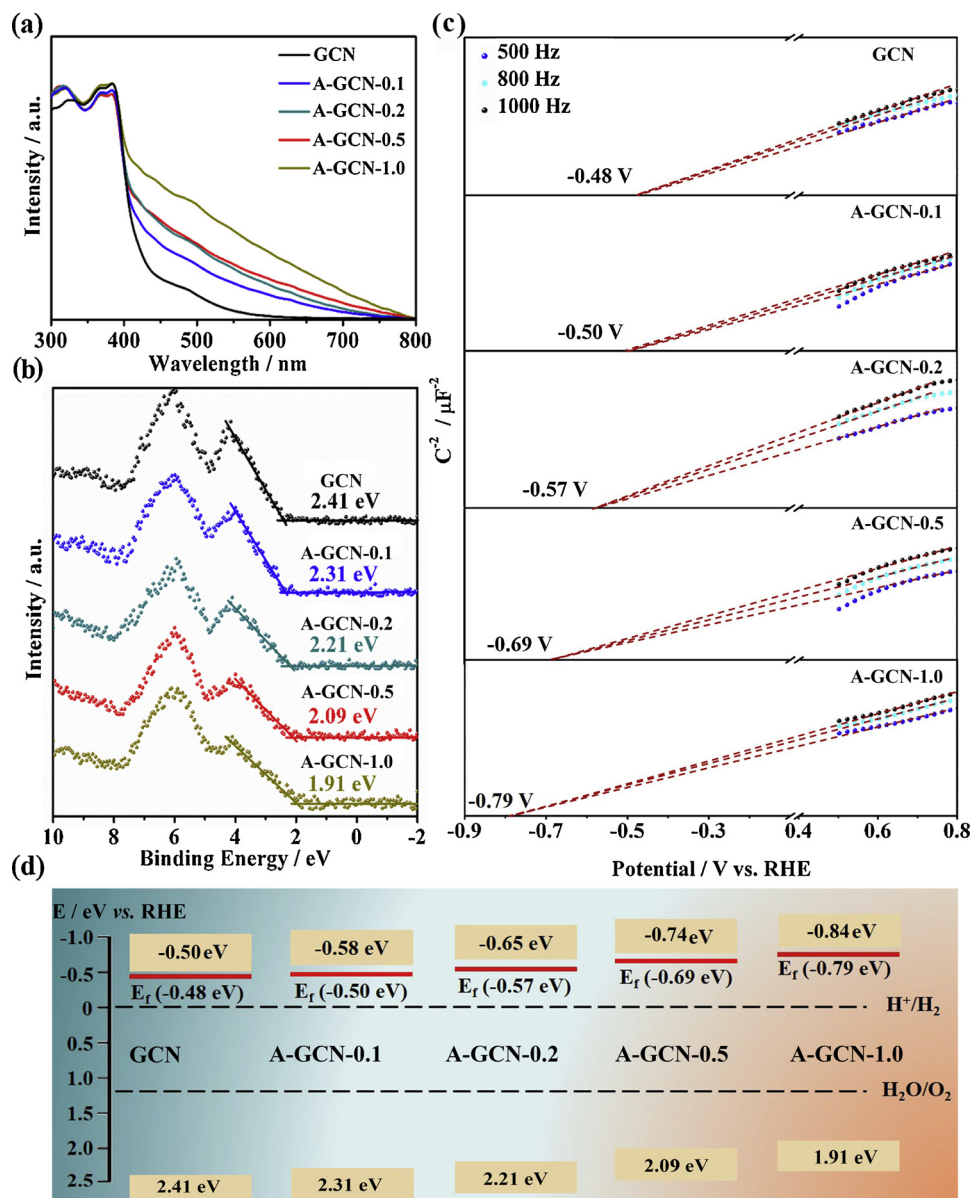


Fig. 4. (a) UV-vis spectra, (b) VB-XPS spectra, (c) Mott-Schottky plot of GCN, A-GCN-0.1, A-GCN-0.2, A-GCN-0.5, and A-GCN-1.0, and (d) schematic illustration of the band structures. The red lines represent Fermi levels. The light yellow bands represent CBs and VBs.

shortcomings (lower interelectrons exchange-correlation) of the generalized gradient approximation (GGA) functional [38]. In detail, the bandgaps of A-GCN-*n* decreases from 2.91 eV to 2.75 eV with the increase of benzene ring embedding amount. The valence band is investigated to characterize the change of energy bands after embedding benzene ring. As shown in Fig. 4b, they appear respectively at about 2.41, 2.31, 2.21, 2.09 and 1.91 eV for GCN, A-GCN-0.1, A-GCN-0.2, A-GCN-0.5, and A-GCN-1.0 (vs. RHE) by conducting VB-XPS. The valence band position gradually shifts up with increasing of benzene ring embedding amount, indicating the change of electronic structure of GCN due to the benzene ring embedding. The flat-band potentials of the samples are measured by the Mott-Schottky plots in Fig. 4c. The type of semiconductor of the material embedded in the benzene ring is remained as n-type. The tangent to the Mott-Schottky curve at different frequencies (500 Hz, 800 Hz, 1000 Hz) intersects at one point, showing the flat band potential of samples that represents the Fermi level positions [39]. The Fermi level position of A-GCN-*n* showed an upward trend corresponding to the increasing amount of terephthalonitrile. According to the flat-band potentials, Fermi levels are estimated to be

-0.48, -0.50, -0.57, -0.69, and -0.79 V (vs. NHE) for GCN, A-GCN-0.1, A-GCN-0.2, A-GCN-0.5, and A-GCN-1.0, respectively. Combining bandgaps characterization of UV-vis spectrum (Fig. 4a), the final band structure is obtained as shown in Fig. 4d by calculating their energy band. The position of the conduction band becomes more negative with the increasing amount of benzene ring embedded, which facilitates the hydrogen evolution due to a greater potential.

3.4. Photogenerated carrier separation and lifetime

The photocatalytic reaction happens on the surface/interface of catalysts involving photogenerated carriers. The lifetime of photogenerated carriers is essential for catalytic performances. Steady-state and transient fluorescence spectra are used to study the lifetime of photocatalytic photogenerated carriers as shown in Fig. 5a. With the increase of the benzene ring embedding amount, the fluorescence signal gradually weakens, which reflects the effective separation of photogenerated carriers. Compared with the material GCN, there is a new peak at 425 nm, which is attributed to the transition change of the band

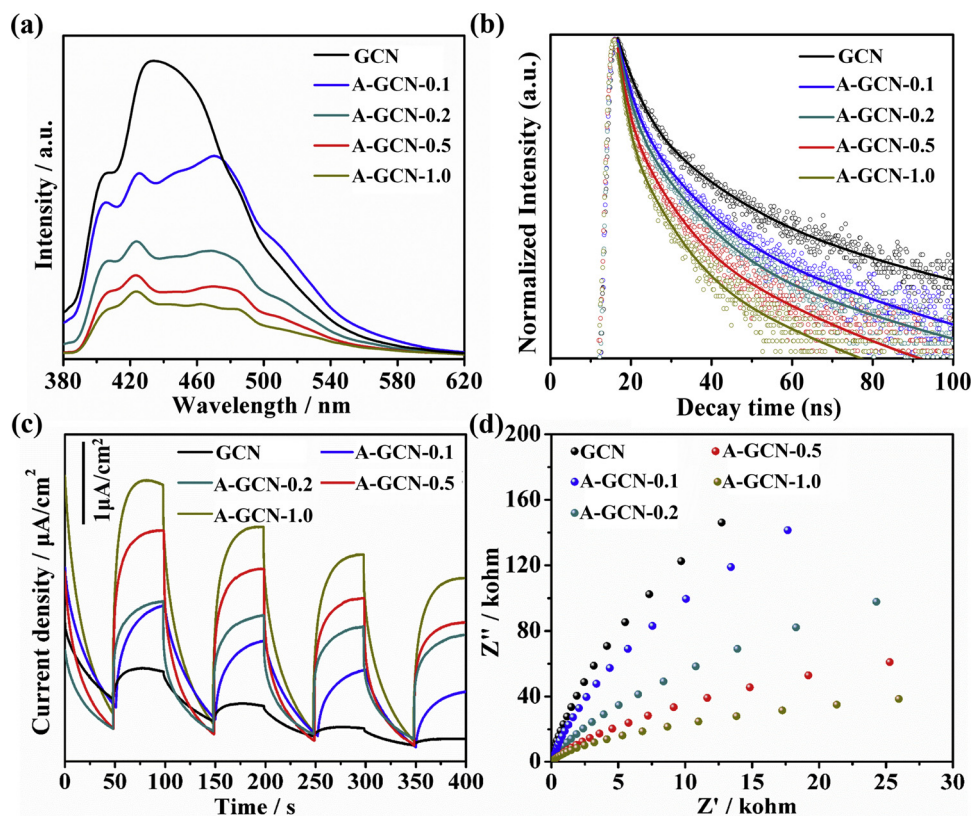


Fig. 5. (a) PL spectra, (b) TRPL spectra and (c, d) electrochemical measurement of GCN, A-GCN-0.1, A-GCN-0.2, A-GCN-0.5, and A-GCN-1.0.

caused by benzene ring embedding. Another distinct peak at 475 nm is due to $n-\pi^*$ electron transition, implying that the benzene embedding acts as the charge-trapping site accelerating electron transfer [26,40]. Furthermore, the transient fluorescence spectra are conducted to understand the exciton separation behavior, and the curves are fitted a three-exponential as shown in Fig. 5b [41]. The fitted slow decay time τ_1 , fast decay time τ_2 and τ_3 , and average lifetime τ_{avg} are summarized in Table S3. The results show that PL lifetime is shortened with the increase of the benzene embedding amount. The observed average lifetimes are 11.25, 7.86, 7.33, 6.11, and 5.38 ns for GCN, A-GCN-0.1, A-GCN-0.2, A-GCN-0.5, and A-GCN-1.0, respectively. The lifetime of A-GCN-1.0 (11.25 ns) is 2.1 times smaller than that of the original GCN (5.38 ns). The shortened lifetime in A-GCN- n indicates the emergence of a non-radiative pathway, which is because the delocalization of electrons from heptazine unit to benzene-ring is enhanced. More carriers were separated to the solid-liquid interface and then accelerate the photocatalytic water splitting reaction. The superior photoelectrochemical performances of A-GCN- n photocathode are demonstrated by measuring the photocurrent under visible-light irradiation ($\lambda > 420$ nm) as shown in Fig. 5c. When the embedded benzene ring gradually increases, the corresponding photocurrent shows a trend of increase, benefitting from the slight red-shift of optical absorption, the effective charge separation and the enhanced charge-carrier lifetime. Electrochemical impedance spectra (EIS) are also measured under visible-light irradiation ($\lambda > 420$ nm) in Fig. 5d. The charge-transfer resistance can be represented as the diameters of the semicircle of EIS. The charge transfer impedance of A-GCN- n is high because of their poor electrical conductivity [42]. The impedance gradually becomes small with the increase of the benzene ring embedding amount, which indicates the photogenerated carriers transport rate is increased, further illustrating the advanced charge carrier behavior.

3.5. Photocatalytic hydrogen production

The H_2 evolution activities of as-prepared catalysts are investigated under visible-light irradiation ($\lambda > 420$ nm). Not surprisingly, the GCN shows the inferior performance of hydrogen ($80.4\ \mu\text{mol}/\text{h}/\text{g}$), and the A-GCN- n displays continuous increasing H_2 evolution as shown in Fig. 6a. The rate of hydrogen production increases with benzene rings embedding. The optimal hydrogen production rate is of $865.1\ \mu\text{mol}/\text{h}/\text{g}$ for A-GCN-1.0, which is 10.8 times larger than that of GCN (Table S4), which is superior to previously reported works (Table S5). The catalysts show good stability and reusability after three cycles of tests. In order to further characterize the stability of the catalyst, we study the structure and morphology of A-GCN before and after the reaction by XRD (Fig. S8) and TEM (Fig. S9). It can be seen that there are no significant changes in terms of structure and morphology before and after the reaction. When the terephthalonitrile amount was further increased, A-GCN-2.0 shows an inferior hydrogen evolution performance (Fig. S10). Control experiments in the dark (or in the absence of catalysts) shows no H_2 releasing, indicating that the H_2 evolution is a photo-driven process and catalyzed by photocatalysts (Fig. S11). Apparent quantum yield (AQY) measurements of A-GCN-1.0 are conducted at a different wavelength in Fig. 6b. The AQY decreases with increasing wavelength, which indicates the wavelength-dependent AQY variation trend is nearly consistent with the absorbance spectrum, and the AQY is 11.3% at 400 nm and 9% at 420 nm.

4. Conclusions

In summary, we synthesized the localized asymmetric graphitized carbon nitride (A-GCN) by embedding benzene rings. The A-GCN exhibits an excellent photocatalytic hydrogen production at a rate of $865.1\ \mu\text{mol}/\text{h}/\text{g}$, 10.8 times higher than that of the GCN ($80.4\ \mu\text{mol}/\text{h}/\text{g}$). Combining experimental and theoretical calculation results, we conclude that the improvement of hydrogen production properties is

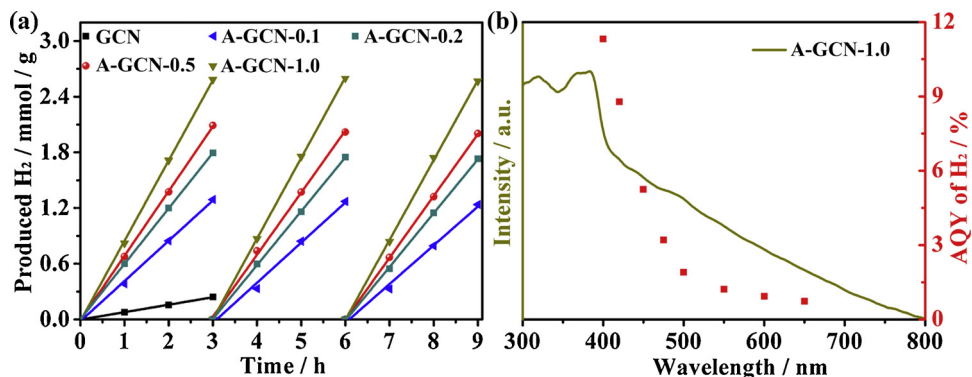


Fig. 6. (a) Typical time course of H_2 evolution rates from water with 10 vol% TEOA under visible light ($\lambda \geq 420$ nm) with 3 wt% Pt co-catalysts and (b) apparent quantum yield (AQY) measurements of H_2 of A-GCN-1.0 at different wavelengths.

mainly attributed to the effective separation of the photogenerated carriers due to the localized asymmetric charge distribution. Therefore, our work shows the localized asymmetry embedding of benzene rings plays an important role in adjusting the electronic structure of two-dimensional carbon-nitrogen materials, which is essential for the design and modification of materials.

Declaration of Competing Interest

None.

Acknowledgments

We greatly acknowledge the National Key Research and Development Program of China (2016YFA0200400), the National Natural Science Foundation of China (51571100, 51872116, 51702116, and 51602305), the National Postdoctoral Program for Innovative Talents (BX20180117), and the Program for JLUSIIRT, 2017TD-09.

Appendix A. Supplementary data

Supplementary material related to this article can be found, in the online version, at doi:<https://doi.org/10.1016/j.apcatb.2019.117959>.

References

- [1] Y. Tachibana, L. Vayssières, J.R. Durrant, *Nat. Photonics* 6 (2012) 511.
- [2] P.D. Tran, L.H. Wong, J. Barber, J.S.C. Loo, *Energy Environ. Sci.* 5 (2012) 5902–5918.
- [3] A. Kudo, Y. Miseki, *Chem. Soc. Rev.* 38 (2009) 253–278.
- [4] L. Liang, X.D. Li, Y.F. Sun, Y.L. Tan, X.C. Jiao, H.X. Ju, Z.M. Qi, J.F. Zhu, Y. Xie, *Joule* 2 (2018) 1004–1016.
- [5] B. Tian, B.N. Tian, B. Smith, M.C. Scott, R.N. Hua, Q. Lei, Y. Tian, *Nat. Commun.* 9 (2018) 1397.
- [6] S.S. Chen, T. Takata, K. Domen, *Nat. Rev. Mater.* 2 (2017) 17050.
- [7] G. Liu, L. Ma, L.C. Yin, G.D. Wan, H.Z. Zhu, C. Zhen, Y.Q. Yang, Y. Liang, J. Tan, H.M. Cheng, *Joule* 2 (2018) 1095–1107.
- [8] M.Q. Yang, Y.J. Xu, W.H. Lu, K.Y. Zeng, H. Zhu, Q.H. Xu, G.W. Ho, *Nat. Commun.* 8 (2017) 14224.
- [9] L. Wang, M.J. Cai, W. Sun, L. He, X.H. Zhang, *Adv. Mater. Interfaces* 5 (2018) 1701694.
- [10] S. Cao, Y. Chen, H. Wang, J. Chen, X.H. Shi, H.M. Li, P. Cheng, X.F. Liu, M. Liu, L.Y. Piao, *Joule* 2 (2018) 549–557.
- [11] J.R. Ran, G.P. Gao, F.T. Li, T.Y. Ma, A.J. Du, S.Z. Qiao, *Nat. Commun.* 8 (2017) 13907.
- [12] J.R. Ran, M. Jaroniec, S.Z. Qiao, *Adv. Mater.* 30 (2018) 1704649.
- [13] J. Liu, Y. Liu, N.Y. Liu, Y.Z. Han, X. Zhang, H. Huang, Y. Lifshitz, S.T. Lee, J. Zhong, Z.H. Kang, *Science* 347 (2015) 970–974.
- [14] T. Song, P.Y. Zhang, T.T. Wang, A. Ali, H.P. Zeng, *Appl. Catal. B Environ.* 224 (2018) 877–885.
- [15] L.H. Lin, W. Ren, C. Wang, A.M. Asiri, J. Zhang, X.C. Wang, *Appl. Catal. B Environ.* 231 (2018) 234–241.
- [16] X.L. Yang, F.F. Qian, G.J. Zou, M.L. Li, J.R. Lu, Y.M. Li, M.T. Bao, *Appl. Catal. B Environ.* 193 (2016) 22–35.
- [17] P. Hu, C.J. Chen, R. Zeng, J.W. Xiang, Y. Huang, D.F. Hou, Q. Li, Y.H. Huang, *Nano Energy* 50 (2018) 376–382.
- [18] W. Che, W.R. Cheng, T. Yao, F.M. Tang, W. Liu, H. Su, Y.Y. Huang, Q.H. Liu, J.K. Liu, F.C. Hu, Z.Y. Pan, Z.H. Sun, S.Q. Wei, *J. Am. Chem. Soc.* 139 (2017) 3021–3026.
- [19] I.F. Teixeira, E.C.M. Barbosa, S.C.E. Tsang, P.H.C. Camargo, *Chem. Soc. Rev.* 47 (2018) 7783–7817.
- [20] S.F. Kang, L. Zhang, C.C. Yin, Y.G. Li, L.F. Cui, Y.G. Wang, *Appl. Catal. B Environ.* 211 (2017) 266–274.
- [21] W.J. Ong, L.L. Tan, Y.H. Ng, S.T. Yong, S.P. Chai, *Chem. Rev.* 116 (2016) 7159–7329.
- [22] H.J. Yu, L. Shang, T. Bian, R. Shi, G.I.N. Waterhouse, Y.F. Zhao, C. Zhou, L.Z. Wu, C.H. Tung, T.R. Zhang, *Adv. Mater.* 28 (2016) 5080–5086.
- [23] G.G. Zhang, Z.A. Lan, L.H. Lin, S. Lin, X.C. Wang, *Chem. Sci.* 7 (2016) 3062–3066.
- [24] Y. Yu, W. Yan, X.F. Wang, P. Li, W.Y. Gao, H.H. Zou, S.M. Wu, K.J. Ding, *Adv. Mater.* 30 (2018) 1705060.
- [25] J. Liu, Y. Yu, R.L. Qi, C.Y. Cao, X.Y. Liu, Y.J. Zheng, W.G. Song, *Appl. Catal. B Environ.* 244 (2019) 459–464.
- [26] Y. Yu, W. Yan, W.Y. Gao, P. Li, X.F. Wang, S.M. Wu, W.G. Song, K.J. Ding, *J. Mater. Chem. A* 5 (2017) 17199–17203.
- [27] Z. Zhu, X. Tang, T.S. Wang, W.Q. Fan, Z. Liu, C.X. Li, P.W. Huo, Y.S. Yan, *Appl. Catal. B Environ.* 241 (2019) 319–328.
- [28] J. Li, D.D. Wu, J. Iocozzia, H.W. Du, X.Q. Liu, Y.P. Yuan, W. Zhou, Z. Li, Z.M. Xue, Z.Q. Lin, *Angew. Chem. Int. Ed.* 58 (2019) 1985–1989.
- [29] J.S. Zhang, G.G. Zhang, X.F. Chen, S. Lin, L. Möhlmann, G. Dołęga, G. Lipner, M. Antonietti, S. Blechert, X.C. Wang, *Angew. Chem. Int. Ed.* 51 (2012) 3183–3187.
- [30] H.J. Yu, R. Shi, Y.X. Zhao, T. Bian, Y.F. Zhao, C. Zhou, G.I.N. Waterhouse, L.Z. Wu, C.H. Tung, T.R. Zhang, *Adv. Mater.* 29 (2017) 1605148.
- [31] B. Lin, G.D. Yang, B.L. Yang, Y.X. Zhao, *Appl. Catal. B Environ.* 198 (2016) 276–285.
- [32] W.N. Xing, C.M. Li, G. Chen, Z.H. Han, Y.S. Zhou, Y.D. Hu, Q.Q. Meng, *Appl. Catal. B Environ.* 203 (2017) 65–71.
- [33] M.S. Zhu, S. Kim, L. Mao, M. Fujitsuka, J.Y. Zhang, X.C. Wang, T. Majima, *J. Am. Chem. Soc.* 139 (2017) 13234–13242.
- [34] C.C. Dong, Z.Y. Ma, R.T. Qie, X.H. Guo, C.H. Li, R.J. Wang, Y.L. Shi, B. Dai, X. Jia, *Appl. Catal. B Environ.* 217 (2017) 629–636.
- [35] I.Y. Kim, S. Kim, Y.J. Jin, S. Premkumar, G. Chandra, N.S. Lee, G.P. Mane, S.J. Hwang, S. Umapathy, A. Vinu, *Angew. Chem. Int. Ed.* 57 (2018) 17135–17140.
- [36] J.Y. Lee, O. Buyukcakir, T.W. Kwon, A. Coskun, *J. Am. Chem. Soc.* 140 (2018) 10937–10940.
- [37] G.G. Zhang, A. Savateev, Y.B. Zhao, L.N. Li, M. Antonietti, *J. Mater. Chem. A* 5 (2017) 12723–12728.
- [38] C. Stampfli, C.G. Van de Walle, *Phys. Rev. B* 59 (1999) 5521–5535.
- [39] Z.Y. Lin, C. Du, B. Yan, C.X. Wang, G.W. Yang, *Nat. Commun.* 9 (2018) 4036.
- [40] H.J. Kim, S.J. Gim, T.H. Jeon, H.J. Kim, W.Y. Choi, *ACS Appl. Mater. Interfaces* 9 (2017) 40360–40368.
- [41] Y. Wang, X.Q. Liu, J. Liu, B. Han, X.Q. Hu, F. Yang, Z.W. Xu, Y.C. Li, S.R. Jia, Z. Li, Y.L. Zhao, *Angew. Chem. Int. Ed.* 57 (2018) 5765–5771.
- [42] X.Q. Fan, L.X. Zhang, R.L. Cheng, M. Wang, M.L. Li, Y.J. Zhou, J.L. Shi, *ACS Catal.* 5 (2015) 5008–5015.